Research Square

Preprints are preliminary reports that have not undergone peer review.
They should not be considered conclusive, used to inform clinical practice,
or referenced by the media as validated information.

High-Pressure Water-Jet Impact on Coal: An SPH-Based Study of Fracture Evolution and Jet-Parameter Effects

Xue Chengchun
China University of Mining and Technology
Hu Yang
huyn1203@163.com

Research Institute of Yunnan Yuntianhua Co., Ltd.
Cao Anye
China University of Mining and Technology
Peng Yujie
China University of Mining and Technology
JIA Liangliang
Mataihao Coal Mine, Ordos Yongmei Mining Co., Ltd. of Inner Mongolia

Article

Keywords: high-pressure water jet, rock burst, pressure relief slotting, crack evolution, parameter optimization, SPH numerical simulation

Posted Date: November 18th, 2026

DOI: https://doi.org/10.21203/rs.3.rs-11575376/v1

License: This work is licensed under a Creative Commons Attribution 4.0 International License.
Read Full License

Additional Declarations: No competing interests reported.

High-Pressure Water-Jet Impact on Coal: An SPH-Based Study of Fracture Evolution and Jet-Parameter Effects

Xue Chengchun[1], *Hu Yang*[2*], *Cao Anye*[1], *Peng Yujie*[1], JIA Liangliang[3]

(1.School of Mines, China University of Mining and Technology, Xuzhou 221116, China;

2.Research Institute of Yunnan Yuntianhua Co., Ltd., Kunming 650600, China;

3.Mataihao Coal Mine, Ordos Yongmei Mining Co., Ltd. of Inner Mongolia, Ordos 017200, China)

* Corresponding author: Hu Yang; E-mail: huyn1203@163.com

Abstract: Jet operating conditions govern fracture development during high-pressure water-jet impact on coal. We combined a first-order analytical model, smoothed particle hydrodynamics (SPH) simulations and field monitoring to examine the effects of working pressure, outlet diameter, incident angle and stand-off distance. The model estimates nominal mean normal impact pressure, while the simulations resolve four stages of damage: surface crushing, main crack propagation, lateral crack initiation and fracture network formation. The analytical pressure threshold of 47.1 MPa falls within the simulated transition interval of 40–60 MPa. By contrast, the analytical incident-angle threshold of 28° is below the simulated transition interval of 45°–60°. Increasing pressure and diameter enlarged crack width and rectangular-equivalent damage area, although maximum crack depth declined slightly at the highest tested levels. Normal incidence produced the most developed fracture network, and a 12 mm stand-off distance maximized the damage dimensions among the tested distances. In the field case, total microseismic energy decreased by 38.96%, and the proportion of high-energy events fell from 25.0% to 15.8% between the weeks before and after slotting. These findings link jet parameters to fracture development and provide screening guidance for selecting slotting conditions.

Key Words: high-pressure water jet; rock burst; pressure relief slotting; crack evolution; parameter optimization; SPH numerical simulation

Introduction

Deep coal mining exposes roadways to high stresses and mining disturbances, increasing the difficulty of controlling coal and rock dynamic failures[1-2]. Pressure-relief measures seek to redistribute stress and release stored elastic energy through controlled coal fracture[3-4]. Selecting effective treatment parameters requires an understanding of how the applied load governs fracture initiation and growth.

High-pressure water jet slotting for pressure relief can directionally induce coal fracture propagation and form continuous slots. By reconstructing the stress field of roadway side surrounding rock to release elastic energy, it promotes the transfer of the original single-peak high stress into the deep coal mass and gradually releases coal elastic energy[5-6]. Previous research has examined coal-breaking mechanisms, stress evolution and the effects of jet parameters. In terms of coal breaking process and mechanism, Wang et al.[7] argued that water jet rock breaking consists of four stages: surface impact, impact pit initiation, impact pit propagation, and impact stagnation. Gao et al.[8] found that the failure of coal-rock mass by water jet results from the combined action of external jet impact load and internal pore pressure load. In terms of stress evolution and fracture propagation, Huang et al.[9] concluded that the wave intensity decreases significantly after stress waves transmit into the slot, effectively reducing the damage of impact load to excavation space. Feng et al.[10] found that the damage zone of the crushing pit decreases with increasing coal-rock strength and porosity, and Liu et al.[11] pointed out that the degree of rock failure decreases with increasing stand-off distance, and the radial cracks generated by impact propagate asymmetrically. In terms of parameter influence laws, Yuan et al.[12] found that changing the jet angle can significantly alter the jet cutting ability; Xu et al.[13] experimentally found that increasing jet pressure promotes the growth of coal damage elements; Zhang et al.[14] numerically found that with increasing water jet diameter, the impact pit expands both in depth and laterally, but the deep expansion trend gradually slows down.

The engineering challenge is to connect these mechanisms and parameter effects within a consistent framework for selecting operating conditions. This requires a defined coal-failure criterion and a comparison between analytical thresholds and simulated damage transitions across pressure, diameter, angle and stand-off distance.

We combine jet dynamics and coal strength in a piecewise analytical model for screening operating conditions, including velocity attenuation beyond the potential-flow core. An SPH model with a JH-2 constitutive description of coal resolves crack development and stress evolution under one-factor-at-a-time parameter variations. Comparing the analytical estimates with these simulations identifies where the screening model captures damage transitions and where its predictions diverge. A field application extends the analysis to microseismic observations during one week before and one week after slotting.

1. Theoretical framework for jet-induced coal breakage

1.1. Mechanisms of jet-induced coal failure

1.1.1. Mechanical effects of jet impact

The core of coal breaking by high-pressure water jet impact can be summarized as three sequentially progressive mechanical effects: water hammer impact, stagnation erosion, and water wedge splitting[15], which constitute a transient dynamic process of hydrodynamic and coal-rock damage coupling (Fig. 1). At the instant of jet contact with the coal mass, the sudden velocity drop generates a high-pressure water hammer, whose magnitude far exceeds the compressive strength of coal, directly causing compressive crushing of the coal in the contact zone. Meanwhile, spherical stress waves propagate into the deep mass and induce tensile stress, triggering initial failure. In the stable impact stage, the stagnation pressure and radial wall jet shear stress jointly erode the coal mass. Through the wedge penetration effect, the stress concentration at crack tips is intensified, driving crack propagation, bifurcation, and coalescence to form a large-scale fracture network. The three effects of water hammer impact, stagnation erosion, and water wedge splitting are spatiotemporally coupled, jointly constituting the mechanical system of coal breaking by high-pressure water jet.

1.1.2. Shear-induced failure mechanism and strength criterion

According to rock mass mechanics theory, the compressive strength of coal is much higher than its shear strength. At the instant of high-pressure water jet impact on coal, the coal in the impact zone is under a complex stress state. Under the combined action of radial and tangential stresses, shear failure occurs when the shear stress exceeds the inherent shear strength of the coal. Based on the Mohr-Coulomb strength theory, a failure criterion for coal shear failure under high-pressure water jet action can be established[16]:

$$D_S = \frac{\sigma_1 - \sigma_3}{2C\cos\varphi + (\sigma_1 + \sigma_3)\sin\varphi} \tag{1}$$

where: Ds is the shear failure criterion coefficient; σ_1 is the maximum principal stress, MPa; σ_3 is the minimum principal stress, MPa; φ is the internal friction angle of coal, °; C is the cohesion of coal, MPa.

When Ds < 1, no shear failure occurs in the coal; when Ds ≥ 1, shear failure occurs. The stagnation pressure and radial shear flow formed by the high-pressure water jet are the main driving forces for inducing coal shear failure, and also the core mechanism for the formation and expansion of the crushing pit.

1.1.3. Tensile failure mechanism and strength criterion

The tensile strength of coal is much lower than its compressive strength, and tensile failure is the main form of fracture development in coal under jet impact. During high-pressure water jet impact, stress waves propagate into the coal interior and reflect at fractures and defects, generating hoop tensile stress around the impact zone. Meanwhile, high-pressure water penetrating into cracks exerts a water wedge action, further intensifying the tensile stress concentration at crack tips. When the tensile stress exceeds the inherent tensile strength of coal, tensile failure occurs, and its failure criterion[17] is:

$$D_t = \frac{\sigma_{tmax}}{\sigma_{tz}} \tag{2}$$

where: Dt is the tensile failure criterion coefficient; σ_{tz} is the hoop tensile stress applied to the coal, MPa; σ_{tmax} is the uniaxial tensile strength of coal, MPa.

When Dt < 1, no tensile failure occurs in the coal; when Dt ≥ 1, tensile failure occurs. Tensile failure is the core mechanism for the extensive development of secondary cracks and the expansion and coalescence of fracture networks inside the coal, directly determining

the pressure relief range and effect around the slot.

1.2. Theoretical model for critical jet parameters

1.2.1. Jet-impact mechanics and the critical coal-breakage criterion

For an ideal incompressible steady water flow, the total mechanical energy remains constant, and the gravitational potential energy term is negligible. Based on the classical Bernoulli equation[18], the water pressure-velocity relationship at the nozzle inlet and outlet can be established:

$$\frac{P_{\text{ent}}}{\rho_{\text{s}}}+\frac{V_{\text{ent}}^2}{2}=\frac{P_{\text{out}}}{\rho_{\text{s}}}+\frac{V_{\text{out}}^2}{2} \tag{3}$$

where: P_{ent} and P_{out} are the water pressures at the nozzle inlet and outlet, respectively, MPa; ρs is the water jet density, which is a constant; V_{ent} and V_{out} are the water jet velocities at the nozzle inlet and outlet, respectively, in m/s.

Substituting the circular cross-sectional area formula into the continuity equation for incompressible steady flow[16], the velocity-diameter relationship at the nozzle inlet and outlet can be obtained:

$$V_{\text{ent}}\cdot\frac{D_{\text{ent}}^2}{4}=\frac{D_{\text{out}}^2}{4}\cdot V_{\text{out}} \tag{4}$$

where: D_{ent} and D_{out} are the nozzle inlet and outlet diameters, respectively.

Combining equations (3) and (4) yields:

$$\rho_{\text{s}}\cdot V_{\text{out}}^2\cdot\left[1-\left(D_{\text{out}}/D_{\text{ent}}\right)^4\right]=2\left(P_{\text{ent}}-P_{\text{out}}\right) \tag{5}$$

Under engineering conditions, $P_{\text{ent}}\gg P_{\text{out}}$ and $(D_{\text{out}}/D_{\text{ent}})^4\ll 1$ are satisfied. Simplifying equation (3), the nozzle outlet velocity V_{out} relationship is obtained:

$$V_{\text{out}}=\sqrt{\frac{2P_{\text{ent}}}{\rho_{\text{s}}}} \tag{6}$$

According to the fluid continuity equation[19], the mass flow rate $\dot{m}$ at the nozzle outlet cross-section is constant. When the air entrainment effect is neglected, the total mass flow rate of the jet remains constant along the path. Substituting the nozzle outlet velocity and eliminating variables, its expression is:

$$\dot{m}=\frac{\pi D_{\text{out}}^2}{4}\sqrt{2\rho_{\text{s}}P_{\text{ent}}} \tag{7}$$

where: $\dot{m}$ is the mass flow rate, kg/s.

In actual working conditions, when the jet reaches the coal surface through the air section, its momentum attenuates along the path due to air resistance and turbulent mixing, and the attenuation degree is directly related to the stand-off distance. The stand-off distance l is measured along the jet axis from the nozzle outlet to its intersection with the coal surface. According to the zonal theory of circular turbulent free jet flow field[20], the length of the potential flow core region of a low-turbulence contraction nozzle is approximately 6.2 times the nozzle diameter. Based on this, a segmented axial velocity attenuation model is established: when the stand-off distance satisfies $l \le 6.2D_{\text{out}}$, the jet is in the potential flow core region, the axial velocity remains equal to the initial nozzle outlet velocity, and the air attenuation effect can be neglected. When the stand-off distance satisfies $l > 6.2D_{\text{out}}$, the jet enters the fully developed main region, and the axial velocity attenuates along the path. The classical empirical formula for the axial velocity in the main region of a circular turbulent jet is adopted to describe its velocity attenuation law. Defining the angle between the jet axis and the coal surface as the incident angle θ ($0° < \theta \le 90°$), and neglecting the normal momentum component caused by water jet rebound, substituting into the nozzle outlet velocity formula yields the effective impact normal velocity at stand-off distance l:

$$V_{l,n}=\begin{cases}\sqrt{\dfrac{2P_{\text{ent}}}{\rho_{\text{s}}}}\sin\theta, & l\le 6.2D_{\text{out}}\\[2ex] \dfrac{0.48D_{\text{out}}}{al+0.147D_{\text{out}}}\sqrt{\dfrac{2P_{\text{ent}}}{\rho_{\text{s}}}}\sin\theta, & l>6.2D_{\text{out}}\end{cases} \tag{8}$$

where: a is the turbulence coefficient, characterizing the jet mixing intensity (engineering value range: 0.055–0.08).

Before the jet impacts the coal wall, the normal momentum flow rate is $\dot{m}V_{l,n}$; after impact, the fluid spreads along the wall as a wall jet, the normal velocity drops to 0, and the normal momentum becomes 0. According to the fluid momentum theorem, the resultant external force on the control volume equals the rate of momentum change of the control volume per unit time, yielding the reaction force of the coal wall on the water flow:

$$F_{c,l}^{'}=\dot{m}\left(0-V_{l,n}\right)=-\frac{\pi D_{\text{out}}^2}{4}\sqrt{2\rho_{\text{s}}P_{\text{ent}}}V_{l,n} \tag{9}$$

where: the negative sign indicates that the reaction force direction is opposite to the normal impact direction of the incoming flow. According to Newton's third law, the actual normal impact force $F_{c,l}$ of the water jet on the coal wall is equal in magnitude and opposite

in direction to the reaction force; taking the positive value:

$$F_{c,l} = \frac{\pi D_{\text{out}}^2}{4}\sqrt{2\rho_s P_{\text{ent}}}V_{l,n} \tag{10}$$

Under normal incidence, the impingement region transitions radially into a wall jet. Lu et al.[21] used the empirical radius relation r/H ≈ 0.22, where H is the nozzle-to-coal distance, and averaged the normal load over the circular area $\pi(0.22\text{H})^2$. Here, H = l and $A_{(l)} = \pi(0.22l)^2$ define the reference area for calculating nominal mean normal pressure. For oblique incidence, the same circular footprint is retained as a geometric approximation. This reference area represents the averaging footprint, distinct from the damaged-coal area and the spatial pressure distribution:

$$A_{(l)} = \pi\left(0.22l\right)^2 \tag{11}$$

Combining the normal impact force formula (10) with the effective impact area formula (11), and substituting into the segmented normal velocity formula (8) to eliminate variables, a unified impact pressure calculation model considering both air dissipation and geometric diffusion is obtained:

$$P_l = \begin{cases} 10.33P_{\text{ent}}sin\theta\left(D_{\text{out}}/l\right)^2, & l \le 6.2D_{\text{out}} \\ \dfrac{4.96D_{\text{out}}^3 P_{\text{ent}}sin\theta}{l^2\left(al+0.147D_{\text{out}}\right)}, & l>6.2D_{\text{out}} \end{cases} \tag{12}$$

Assumptions and scope of the analytical model. The model estimates nominal mean normal impact pressure for comparing operating conditions. It assumes steady, incompressible flow with constant density, negligible gravity and nozzle losses, and outlet pressure small relative to inlet pressure. Jet centreline velocity remains constant within the potential-flow core and follows the empirical decay relation downstream. Mass flow rate is conserved, with air entrainment neglected.

The geometric applicability condition is $0.22l \ge D_{\text{out}}/2$, or $l \ge D_{\text{out}}/0.44$. This condition keeps the assumed impact footprint at least as wide as the nozzle exit and excludes the zero-area singularity at l = 0. The lower bound is derived from the footprint geometry.

The pressure $P_l = F_{c,l}/A_{(l)}$ is the normal load averaged over the prescribed impact footprint. The condition $P_l \ge \sigma_c$ uses the static uniaxial compressive strength as a screening reference. Transient water-hammer pressure, multiaxial and strain-rate effects, tensile crack growth and water-wedge action lie outside this mean-pressure criterion.

1.2.2. Critical nozzle working pressure

The nozzle working pressure controls the initial jet velocity and impact energy. Using the screening condition $P_l \ge \sigma_c$, the analytical estimate of the pressure required to initiate coal damage is obtained as follows:

$$P_{\text{ent}} = \begin{cases} \dfrac{\sigma_c}{10.33sin\theta}\left(l/D_{\text{out}}\right)^2, & l \le 6.2D_{\text{out}} \\ \dfrac{l^2\sigma_c\left(al+0.147D_{\text{out}}\right)}{4.96D_{\text{out}}^3 sin\theta}, & l>6.2D_{\text{out}} \end{cases} \tag{13}$$

1.2.3. Critical nozzle outlet diameter

The nozzle outlet diameter controls jet mass flow rate and nominal impact load. Applying the screening condition $P_l \ge \sigma_c$ gives the outlet-diameter threshold:

$$\begin{cases} \dfrac{10.33P_{\text{ent}}sin\theta D_{\text{out}}^2}{l^2\sigma_c}=1, & l \le 6.2D_{\text{out}} \\ 4.96P_{\text{ent}}sin\theta D_{\text{out}}^3 - 0.147\sigma_c l^2 D_{\text{out}} \\ -a\sigma_c l^3 = 0, & l>6.2D_{\text{out}} \end{cases} \tag{14}$$

1.2.4. Critical jet incident angle

The incident angle sets the normal component of jet momentum. With the footprint approximation defined above, the screening condition $P_l \ge \sigma_c$ gives the corresponding angle threshold:

$$\theta = \begin{cases} \arcsin\left(\dfrac{\sigma_c}{10.33P_{\text{ent}}}\left(\dfrac{l}{D_{\text{out}}}\right)^2\right), & l \le 6.2D_{\text{out}} \\ \arcsin\left(\dfrac{l^2\sigma_c\left(al+0.147D_{\text{out}}\right)}{4.96D_{\text{out}}^3 P_{\text{ent}}}\right), & l>6.2D_{\text{out}} \end{cases} \tag{15}$$

1.2.5. Critical stand-off distance

The stand-off distance controls jet velocity and the assumed impact area. Applying the screening condition $P_l \ge \sigma_c$ gives the maximum effective stand-off distance within the analytical model:

$$\begin{cases} 10.33P_{\text{ent}}sin\theta D_{\text{out}}^2 - l^2\sigma_c=0, & l \le 6.2D_{\text{out}} \\ a\sigma_c l^3 + 0.147\sigma_c D_{\text{out}} l^2 \\ -4.96P_{\text{ent}}sin\theta D_{\text{out}}^3 = 0, & l>6.2D_{\text{out}} \end{cases} \tag{16}$$

For the baseline nozzle diameter of 2.5 mm, the geometric lower bound defined in Section 1.2.1 is 5.68 mm. Analytical pressure estimates therefore cover the sampled distances of 8, 12, 16 and 20 mm. The 0 mm and 4 mm cases are evaluated numerically; both are below the geometric lower bound, and the zero-distance case also gives a singularity in the assumed area expression.

2. SPH model and simulation design

2.1. Smoothed particle hydrodynamics method

and its applicability

The SPH method in LS-DYNA represents the transient interaction between the water jet and coal. SPH discretizes the continuum into particles carrying mass, velocity, stress and other state variables[22]. Its particle formulation accommodates the large deformation, moving interfaces and material separation associated with jet impact and coal fragmentation.

2.2. Material models and parameters

The JH-2 constitutive model[23] is adopted to describe the stress propagation, crack propagation, and dynamic fragmentation process of coal. This model includes three strength states: intact, damaged, and fractured, and characterizes the elastic limit of coal failure by equivalent stress. The normalized strength of each state is:

$$\begin{cases} \sigma_a^* = A(P^* + T^*)^N \times (1 + C\ln\dot{\varepsilon}^*), \ D = 0 \\ \sigma_b^* = B(P^*)^M \times \left(1 + C\ln\dot{\varepsilon}^*\right), \ D = 1 \\ \sigma_c^* = \sigma_a^* - D(\sigma_a^* - \sigma_b^*), 0 < D < 1 \end{cases} \quad (17)$$

where: σ_a^*, σ_b^*, and σ_c^* are the normalized equivalent strengths of coal in intact, fully fractured, and damaged states, respectively; $P^* = P/P_{HEL}$ is the normalized pressure, where P is the actual pressure and P_{HEL} is the pressure at the Hugoniot elastic limit; $T^* = T/P_{HEL}$ is the normalized maximum hydrostatic tensile stress under the hydrostatic tensile limit that the material can withstand, where T is the maximum tensile stress the coal can withstand; C is the strain rate sensitivity coefficient; $\dot{\varepsilon}^* = \dot{\varepsilon}/\dot{\varepsilon}_0$ is the normalized strain rate, where $\dot{\varepsilon}$ is the equivalent plastic strain rate and $\dot{\varepsilon}_0 = 1.0\ s^{-1}$; A and N are rock material parameters; B and M are material parameters under the fully fractured state; D is the coal damage degree, $0 \le D \le 1$. The specific calculation parameters of the JH-2 model in this paper are shown in Table 1.

Table 1 combines physical and mechanical properties from the target-mine testing report with constitutive constants selected by reference to Jiang et al.[24]. That study used SPH/FEA and a rate-dependent JH-2 model for granite under continuous and discontinuous water-jet impact and compared erosion depths and fracture patterns with published experiments. Their work provides a methodological reference for the present impact model.

In studies related to high-pressure water jet coal breaking, a polynomial equation of state is generally adopted to describe the constitutive model of water[25], and its expression is:

$$P_w = \begin{cases} A_1\delta + A_2\delta^2 + A_3\delta^3 \\ +(B_0 + B_1\delta)\rho_w e, \ \delta \ge 0 (\text{Compression}) \\ T_1\delta + T_2\delta^2 + B_0\rho_w e, \ \delta \le 0 (\text{Expansion}) \end{cases} \quad (18)$$

where: P_w is the water jet pressure, Pa; δ is the water jet compression ratio; e is the water jet internal energy, J/kg; ρ_w is the water jet density, kg/m³; $A_1 = T_1 = 2.2$ GPa, $A_2 = 9.54$ GPa, $A_3 = 14.57$ GPa, $T_2 = 0$, B_0 and B_1 are dimensionless material constants, with $B_0 = B_1 = 0.28$, all of which are water medium material constants.

2.3. Numerical model and simulation cases

2.3.1. Model geometry and boundary conditions

The numerical model comprises a 25 mm initial water-jet segment and a coal domain measuring 75 mm × 50 mm (Fig. 3). Both materials are discretized with SPH, totaling 266,300 particles. No additional water particles are introduced during the simulation. Non-reflecting conditions on the lateral and bottom boundaries reduce artificial stress-wave reflections[26], while the top surface interacts freely with the jet. The water and coal are represented in a Lagrangian description[23].

2.3.2. Simulation design

The simulation design uses a coal uniaxial compressive strength of 21.1 MPa and a turbulence coefficient of 0.055. At the baseline nozzle diameter of 2.5 mm, incident angle of 90°, working pressure of 100 MPa and stand-off distance of 12 mm, the analytical screening thresholds are 47.1 MPa for pressure, 1.78 mm for diameter, 28.0° for angle and 16.9 mm for maximum stand-off distance. The sampled parameter levels bracket these estimates to locate simulated damage transitions (Fig. 3). The 16.9 mm estimate uses the downstream velocity-attenuation branch because it exceeds the nominal potential-core length of 15.5 mm.

2.4. Crack quantification and evaluation metrics

The rectangular-equivalent damage area, S_{eq}, was used as a two-dimensional geometric index of the overall damage extent. It was calculated as:

$$S_{eq} = L_{max} \times W_{max} \quad (19)$$

Here, L_{max} is the maximum crack-development depth along the jet axis, and Wmax is the maximum transverse width of the damaged region. Their product defines

the rectangular envelope of the fracture network. The envelope includes intact gaps between branches, so Seq measures two-dimensional damage extent rather than actual fractured area, crack surface area or three-dimensional damage volume.

Cracks were identified by visual inspection of the final damage-field images, with each distinguishable branch counted once. This manual procedure used no numerical damage threshold. Each branch orientation was determined from its principal propagation direction relative to the positive horizontal axis and recorded within 0°–180°. Counts were tabulated at the orientations shown in the plots.

3. Damage and stress evolution under water-jet impact

A representative case with a nozzle diameter of 3.5 mm, working pressure of 120 MPa, incident angle of 90° and stand-off distance of 12.0 mm illustrates the temporal development of damage and stress. Section 4 examines the effects of individual parameters using the baseline conditions defined in Section 2.3.2.

3.1. Damage development and crack propagation

The damage evolution and crack propagation state of coal at different impact moments are shown in Fig. 4, presenting an obvious sequential progression law: 0–1 μs: the instantaneous water hammer pressure far exceeds the compressive strength of coal, shear failure occurs at the impact center point to form a continuous crushing zone, energy is concentrated on the surface, and no obvious cracks exist inside; 1–31 μs: the incident energy propagates to the deep mass in the form of stress waves, a central main crack initiates along the central axis and extends axially, and a small number of radial microcracks appear at the edge of the crushing zone; 31–61 μs: stress waves interact with the developing cracks and concentrate stress near their tips, promoting rapid oblique extension of lateral main cracks on both sides, formation of sub-horizontal cracks, and development of the fracture network; 61–76 μs: the impact energy attenuates, main crack propagation slows down, secondary branch cracks continue to develop, the damage range tends to stabilize, and a symmetric funnel-shaped failure morphology is finally formed. The progression from localized surface crushing to internal crack growth is consistent with the coupled compressive, shear and tensile failure processes described in Section 1.1.

3.2. Stress-wave propagation and evolution in coal

Figure 5 shows the stress field evolving from a localized contact peak into inward and lateral stress waves. During 0–1 μs after initial contact, the simulated local stress reaches 12.6 GPa. This transient value describes the contact-zone response; the analytical model instead evaluates the normal load averaged over its prescribed footprint. During 1–31 μs, tensile stress develops behind the propagating wave front, and a central crack initiates when the coal tensile strength is exceeded. During 31–61 μs, stress concentrations at crack tips accompany lateral and sub-horizontal crack growth. The sequence connects surface crushing with subsequent tensile fracture inside the coal.

4. Effects of nozzle parameters on coal breakage

The effects of pressure, diameter, incident angle and stand-off distance are evaluated using one-factor-at-a-time simulations. The baseline nozzle diameter is 2.5 mm, the working pressure is 100 MPa, the incident angle is 90° and the stand-off distance is 12 mm. The resulting damage transitions are compared with the analytical screening thresholds.

4.1. Effect of nozzle working pressure

Increasing working pressure expands the damaged region and increases fracture complexity (Fig. 6(a)). Six pressures from 20 to 120 MPa were simulated. At 20 MPa, damage is confined mainly to the surface. At 40 MPa, the central crack extends inward with limited lateral growth. At 60 MPa and above, lateral and secondary branches form a more developed fracture network. The analytical threshold of 47.1 MPa lies within this simulated transition interval of 40–60 MPa, resolved at the tested 20 MPa increments.

The crack characteristics at different water-jet pressures are compared in Fig. 6(b) and (c). Crack width and rectangular-equivalent damage area increased across the tested pressures. Maximum crack depth rose from 5.2 mm at 20 MPa to 48.6 mm at 100 MPa, then declined to 43.8 mm at 120 MPa. At 120 MPa, 10 cracks were counted, the maximum width was 46.7 mm, and the rectangular-equivalent damage area was 2045.46 mm². Three of the 10 cracks

were assigned angles between 75° and 105°; the full angular distribution was approximately symmetric.

The pressure trend follows the increase in jet velocity and energy. The Bernoulli relation gives a nozzle velocity proportional to the square root of working pressure. At fixed water volume, increasing pressure raises the initial kinetic energy available for impact and stress-wave propagation. Within the potential-flow core, the analytical mean impact pressure is proportional to working pressure at fixed geometry, linking the applied pressure to the expanding fracture network.

4.2. Effect of nozzle outlet diameter

Increasing nozzle diameter broadens the fracture network (Fig. 7(a)). At 1.0 mm, a central crack dominates, with limited lateral branching. At 1.5 mm, the central crack becomes deeper while lateral growth remains limited. At 2.0 mm and above, lateral and secondary cracks develop alongside the central crack. The largest tested diameter, 3.5 mm, produces the greatest fracture extent and complexity. The analytical diameter threshold of 1.78 mm falls within the simulated transition interval of 1.5–2.0 mm.

The crack characteristics at different nozzle diameters are compared in Fig. 7(b) and (c). Crack width and rectangular-equivalent damage area increased with diameter. Maximum depth reached 49.5 mm at 3.0 mm and was slightly lower, 49.2 mm, at 3.5 mm. At 3.5 mm, 15 cracks were counted, the maximum width was 54.8 mm, and the rectangular-equivalent damage area was 2696.16 mm². Eleven of the 15 cracks were assigned angles from 75° to 150°, indicating a broad angular distribution.

At fixed velocity, jet mass flow rate scales with the square of nozzle diameter. A larger diameter therefore increases incident momentum flux and extends the potential-flow core. These changes increase the loaded region and the energy available for fracture development, consistent with the wider and more branched networks in Fig. 7.

4.3. Effect of jet incident angle

Increasing incident angle from 15° to 90° promotes fracture development, with normal incidence producing the most developed network among the tested cases (Fig. 8). Damage at 15° is concentrated near the surface, and the transition to extensive fracturing occurs between 45° and 60°. The analytical estimate of 28° is 17°–32° below this interval. The discrepancy identifies incident angle as a limitation of the retained normal-incidence footprint approximation.

The crack characteristics at different incidence angles are compared in Fig. 8(b) and (c). Crack depth, width, and rectangular-equivalent damage area increased across the tested angles. At 90°, seven cracks were counted, the maximum depth was 48.6 mm, the maximum width was 28.6 mm, and the rectangular-equivalent damage area was 1389.96 mm². Three of the seven cracks were assigned angles between 75° and 105°. The 90° distribution was approximately symmetric about the central direction.

The normal component of jet momentum increases as the incident angle approaches 90°, increasing the effective normal load. The analytical model represents this momentum change but retains a circular footprint; it therefore omits the angle-dependent impact geometry and asymmetric wall-jet pressure distribution. The simulated trend supports normal incidence for the conditions examined here.

4.4. Effect of stand-off distance

Stand-off distance changes both damage depth and lateral spread (Fig. 9). Across the six tested distances from 0 to 20 mm, the most balanced fracture pattern occurs at 12 mm; the 0 mm case produces wide, shallow damage, and damage dimensions decline at larger distances. The nominal potential-core length is 15.5 mm for the 2.5 mm nozzle, placing the 16 mm case just downstream of the core. Analytical comparisons cover 8–20 mm, while the 0 mm and 4 mm cases are evaluated numerically under the applicability rule in Section 1.2.1. At 20 mm, the model still produces six cracks and a rectangular-equivalent damage area of 918.76 mm². Fracturing therefore persists beyond the analytical screening distance of 16.9 mm.

The crack characteristics at different stand-off distances are compared in Fig. 9(b) and (c). Maximum depth increased from 33.5 mm at 0 mm to 48.6 mm at 12 mm, then decreased to 44.6 mm at 20 mm. Crack width varied across the tested distances, reaching its maximum of 28.6 mm at 12 mm. Rectangular-equivalent damage area first increased from 830.8 mm² at 0 mm to 1389.96 mm² at 12 mm and then decreased to 918.76 mm² at 20 mm. At 12 mm, seven cracks were counted; three of them were assigned angles between 75° and 105°.

The largest measured depth, width and rectangular-equivalent damage area occur at

12 mm, identifying it as the preferred stand-off distance among the tested cases. The shallower damage at shorter distances and the reduction beyond 12 mm reflect changes in axial penetration and lateral fracture development. Jet mixing and velocity attenuation provide a physical interpretation of the decline at larger distances, including the 16 mm and 20 mm cases downstream of the nominal potential-flow core.

4.5. Comparison with published studies and model limitations

The simulated fracture patterns show qualitative correspondence with published water-jet experiments on coal. Xiao et al.[27] observed a damaged pit surrounded by radial and annular cracks, with more severe fragmentation at higher jet velocities. The present simulations similarly show expansion of the damaged region and growth of lateral and secondary cracks as pressure increases. Ge et al.[28] used CT scans after water-jet loading under true triaxial stress and showed that stress conditions affect fracture orientation and damage extent. Together, these comparisons place the simulated trends in the context of experimentally observed coal-fracture behaviour.

The analytical model provides screening thresholds based on nominal mean pressure, while the SPH model resolves damage evolution for the specified geometry, material set and loading conditions. Quantitative prediction errors remain undetermined: the available experiments differ in coal properties, nozzle geometry, stand-off distance, loading and stress state, and no experiment matching the present conditions was conducted. The literature-derived constitutive constants were also used without independent calibration for the target coal. Agreement between analytical and simulated transition intervals therefore measures consistency between the two models; matched experiments are required to establish quantitative accuracy for the thresholds, crack dimensions and counts. The geometric near-field cutoff follows from the assumed footprint and has no experimental calibration. The stress fields support the interpretation of coupled failure processes, while the separate contribution of water-wedge action remains unquantified.

5. Engineering application

5.1. Engineering background and pressure-relief construction parameters

The 730 mining area of a certain mine mainly mines the No.3 coal seam, with an average thickness of 10.2 m, a burial depth of 980–1100 m, a uniaxial compressive strength of coal of 21.1 MPa, and the coal seam has a strong rock burst tendency. The mining area adopts double-wing mining. Affected by the superposition of mining-induced abutment pressure from the two-wing working faces, the concentrated roadways in the mining area have a high degree of stress concentration and strong rock burst risk. After rock burst prevention measures such as floor cutting construction, bottom coal replacement, and borehole pressure relief, local stress concentration has not been fully relieved, and the rock burst risk has not been completely eliminated.

To address the above problems, the mine first introduced high-pressure water jet slotting pressure relief technology for rock burst prevention and control. Combining the theoretical critical criterion derived above with the parameter influence laws obtained from numerical simulation, and targeting the coal seam occurrence conditions and on-site construction conditions of this mine, high-pressure water jet slotting pressure relief measures were implemented on the coal mass at the side of the No.3 crossheading, with a total of 6 pairs of slotting boreholes. A CMS1-1450/30 drill jumbo and a ZGF-100(A) high-pressure water jet slotting device were adopted. The borehole position was 1.5 m from the roadway floor, the borehole diameter was 113 mm, and the borehole was perpendicular to the roadway side, consistent with the coal seam dip angle. The final construction parameters were determined as follows: nozzle outlet diameter of 3.5 mm, construction working pressure of 120 MPa, nozzle incident on the coal wall at 90°, and construction stand-off distance controlled at 12 mm. Cyclic operation was carried out according to the designed borehole depth of 25 m, spacing of 5 m, and slotting step distance of 2 m, so that the slotting range continuously covered the high-stress abnormal zone at the roadway side. The pressure relief layout is shown in Fig. 10.

5.2. Field assessment of pressure-relief effects

Microseismic activity decreased during the week following slotting (Table 2). Construction on both sides of the No.3 crossheading was completed on 20 June 2020; monitoring covered 13–19 June 2020 before treatment and 21–27 June 2020 after treatment.

No event exceeded 10^4 J during the service period of the concentrated roadways in the 730 mining area. Events were classified as high-energy for $E > 10^3$ J and low-energy for $E \leq 10^3$ J. The weekly event count decreased from 28 to 19 (32.1%), and the mean daily count decreased from 4.00 to 2.71 events per day, with the same reduction calculated before rounding. Total energy decreased from 2.49×10^4 J to 1.52×10^4 J (38.96%). High-energy events decreased from 7 to 3 (57.1%), and their proportion fell from 25.0% to 15.8%; the low-energy proportion rose from 75.0% to 84.2%. These changes document lower event frequency and energy after treatment. The seven-day comparison had no control roadway, so the separate contributions of slotting and other mining influences remain unresolved; the observations alone do not establish a causal reduction in rock-burst risk.

6 Conclusions

The analytical, numerical and field investigations yielded the following findings:

(1) The analytical model relates pressure, diameter, incident angle and stand-off distance to nominal mean normal impact pressure. Its pressure and diameter thresholds fall within the corresponding simulated damage-transition intervals. The angle estimate is 17°–32° below the simulated transition interval, and simulated fracturing persists at 20 mm, beyond the estimated 16.9 mm stand-off limit. These comparisons define the performance of the model as a screening tool across the four parameters.

(2) The simulated damage develops through four stages: surface crushing, main crack propagation, lateral crack initiation and fracture network formation. The evolving stress field links localized surface crushing with subsequent internal crack growth, consistent with coupled compressive, shear and tensile failure.

(3) Increasing working pressure and outlet diameter enlarges crack width and rectangular-equivalent damage area across the tested conditions; maximum depth declines slightly at the highest pressure and diameter. Normal incidence produces the most developed fracture pattern among the tested angles. A stand-off distance of 12 mm maximizes depth, width and rectangular-equivalent damage area in the distance series. These results support parameter selection within the simulated ranges.

(4) Field slotting used a 3.5 mm nozzle, a working pressure of 120 MPa, normal incidence and a stand-off distance of 12 mm. Between the monitored weeks before and after treatment, total microseismic energy decreased by 38.96%, and the high-energy event proportion decreased from 25.0% to 15.8%. The field case documents reduced microseismic activity following application of the selected parameters.

Data availability

The numerical data used to generate the figures are provided in Supplementary Data 1. The field-monitoring data supporting the conclusions are reported in Table 2. Additional simulation data and model input files are available from the corresponding author upon reasonable request.

Code availability

The numerical simulations were performed using the commercial software LS-DYNA. The specific model input files (K-files) containing the material parameters, EOS, and boundary conditions are available from the corresponding author upon reasonable request.

Author contributions

X.C. conceived the study, conducted the numerical simulations, performed the data analysis, and drafted the manuscript. H.Y. supervised the study, contributed to the interpretation of the results, and revised the manuscript. All authors discussed the results, critically reviewed the manuscript, and approved the final version for submission.

Funding

This work was sponsored by National Natural Science Foundation of China (52604148, 52604150,52274098), Supported by the Open Fund of the State Key Laboratory of Coalburst Theory and Prevention Technology National Mine Safety Administration(Preparatory)(Grant No. KFJJ-2025-0006).

Competing interests

The authors declare no competing interests.

References

[1] Kang Hongpu, Jiang Pengfei, Yang Jianwei, et al. Theory and complete technology of surrounding rock collaborative control for deep coal mine roadways [J]. Journal of China Coal Society, 2026, 51(1): 60-92. DOI:10.13225/j.cnki.jccs.2025.1488.

[2] Yang Ke, Guo Penghui, Yuan Liang, et al. Research progress on main controlling factors and mechanisms of typical dynamic disaster gestation in deep mining coal mines [J]. Journal of China Coal Society, 2025, 50(7): 3466-3487. DOI:10.13225/j.cnki.jccs.2024.0929.

[3] Yuan Liang, Wang Enyuan, Ma Yankun, et al. Research progress and scientific and technological challenges of coal-rock dynamic disasters in China [J]. Journal of China Coal Society, 2023, 48(5): 1825-1845. DOI:10.13225/j.cnki.jccs.2023.0264.
[4] Zhou Liyuan, Yin Xinxin, Wu Zhen, et al. Review on mechanism of rock burst induced by mine seismicity and collaborative prevention and control technology in deep coal mines[J/OL]. Progress in Geophysics, 1-18[2026-09-07]. https://link.cnki.net/urlid/11.2982.p.20260708.1626.014.
[5] Zhang Yongjiang, Xu Zunyu, Li Shuai, et al. Key technology and application of "slotting-pressure combined" pressure relief and permeability enhancement by ultra-high pressure water jet [J]. Coal Science and Technology, 2025, 53(9): 201-212.
[6] Lu Yiyu, Huang Shan, Ge Zhaolong, et al. Progress and strategic thinking of water jet pressure relief and permeability enhancement technology in coal mines of China [J]. Journal of China Coal Society, 2022, 47(9): 3189-3211. DOI:10.13225/j.cnki.jccs.SS22.0602.
[7] Wang Dong, Li Tie, Liu Meihua, et al. Analysis on influence of pulsed water jet on coal fracture characteristics [J]. Coal Science and Technology, 2025, 53(S2): 116-128.
[8] Gao Yabin, Xiang Xin, Guo Xiaoya, et al. Study on characteristics and mechanism of coal-rock breaking by borehole water jet impact [J]. Journal of Vibration and Shock, 2022, 41(23): 51-59+85. DOI:10.13465/j.cnki.jvs.2022.23.007.
[9] Huang Zhenfei, Zhang Yongjiang. Study on ultra-high pressure water jet slotting pressure relief technology in rock burst coal seams [J]. Coal Engineering, 2026, 58(7): 97-105.
[10] Feng Renjun, Zhu Yongjian, He Jianxin. Damage and failure characteristics and influence analysis of heterogeneous loaded coal-rock impacted by pulsed water jet [J]. Journal of Safety Science and Technology, 2025, 21(2): 90-98.
[11] Liu Hongmei, Wang Wenlong, He Jingqiang, et al. Simulation study on crack damage of uneven rock strata impacted by water jet [J]. Journal of Machine Design and Research, 2026, 42(2): 385-392. DOI:10.13952/j.cnki.jofmdr.2026.0062.
[12] Yuan Ruifu, Qin Bo, Dong Zhuo, et al. Experimental study on influence of abrasive water jet impact angle on sandstone cutting performance [J]. Journal of China Coal Society, 2024, 49(S1): 208-219. DOI:10.13225/j.cnki.jccs.2023.0301.
[13] Xu S ,Zhu Y ,Liu S , et al. Study on the Variation Characteristics and Laws of Hole Formation in Coal-Rock Masses under HPWJ Impact Fracturing.[J].ACS omega,2025,10(45):55082-55097.DOI:10.1021/ACSOMEGA.5C10246.
[14] Zhang Shaoqi, Gao Yabin, Cao Jing, et al. Simulation study on coal-rock damage characteristics induced by borehole water jet impact [J]. Safety in Coal Mines, 2022, 53(10): 97-104. DOI:10.13347/j.cnki.mkaq.2022.10.013.
[15] Zhao Yueran, Jiang Wenzhong, Jin Peng, et al. Research progress and prospect of coal breaking mechanism by high-pressure water jet [J]. Safety in Coal Mines, 2022, 53(4): 183-192. DOI:10.13347/j.cnki.mkaq.2022.04.029.
[16] He Manchao, Xie Heping, Peng Suping, Jiang Yaodong. Study on rock mechanics in deep mining [J]. Chinese Journal of Rock Mechanics and Engineering, 2005(16): 2803-2813.
[17] Yang Shang. Study on high-pressure water jet pressure relief technology for residual coal pillars in overlying goaf of close-distance coal seam mining [D]. Shandong University of Science and Technology, 2020.
[18] Mo Nairong. Engineering Fluid Mechanics[M]. Huazhong University of Science and Technology Press, 2017.
[19] Han Zhanzhong, Wang Jingang. Engineering Fluid Mechanics[M]. 4th ed. Beijing: Beijing Institute of Technology Press, 2019.
[20] Yu Changzhao. Turbulent Jets[M]. Beijing: Higher Education Press, 1993: 32-41.
[21] Lu Yiyu, Liu Yong, Xia Binwei, et al. Optimization analysis and application of borehole layout in cross-cut coal uncovering [J]. Journal of China Coal Society, 2011, 36(2): 283-287. DOI:10.13225/j.cnki.jccs.2011.02.024.
[22] Zhang Qiang, Liu Yang, Tian Ying, et al. SPH simulation study on flow process of automatic top-coal caving based on elastoplastic soil constitutive model [J]. Coal Science and Technology, 2025, 53(S2): 321-335.
[23] Zhang X, Hao H, Ma G. Dynamic material model of annealed soda-lime glass[J]. International Journal of Impact Engineering, 2015, 77: 108-119.
[24] Jiang Hongxiang, Liu Zenghui, Gao Kuidong. Numerical simulation on rock fragmentation by discontinuous water-jet using coupled SPH/FEA method[J]. Powder Technology,2017,312:248-259. doi:10.1016/j.powtec.2017.02.047
[25] Jiang Hongxiang, Du Changlong, Liu Songyong, et al. Analysis of rock breaking damage field under high-pressure water jet impact [J]. Journal of Central South University (Science and Technology), 2015, 46(1): 287-294.
[26] Jiang H, Du C, Liu S, et al. Numerical simulation of rock fragmentation under the impact load of water jet[J]. Shock and Vibration, 2014, 2014: 1-11.
[27] Xiao Songqiang, Ren Qingyang, Guan Ruishi, et al. Theoretical and experimental investigation on fracture response of coal impacted by high-velocity water jet[J]. Energy Reports,2021,7:3210-3224. doi:10.1016/j.egyr.2021.05.029
[28] Ge Zhaolong, Cao Shirong, Lu Yiyu, et al. Fracture mechanism and damage characteristics of coal subjected to a water jet under different triaxial stress conditions[J]. Journal of Petroleum Science and Engineering,2021,208:109157. doi:10.1016/j.petrol.2021.109157

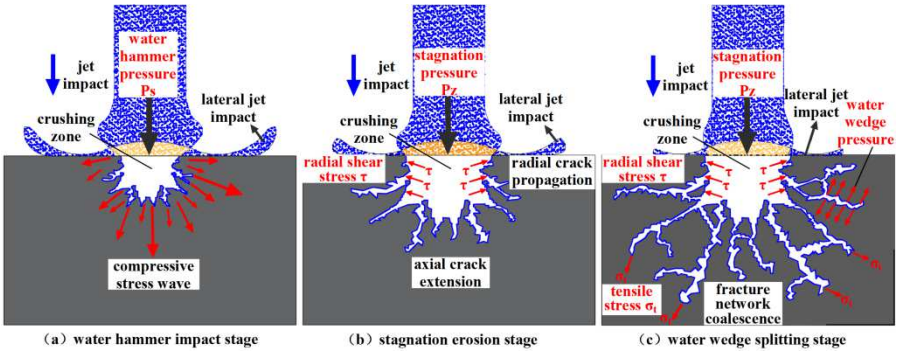


Fig. 1 Schematic diagram of the process and action mechanism of coal breaking under HPWJ impact

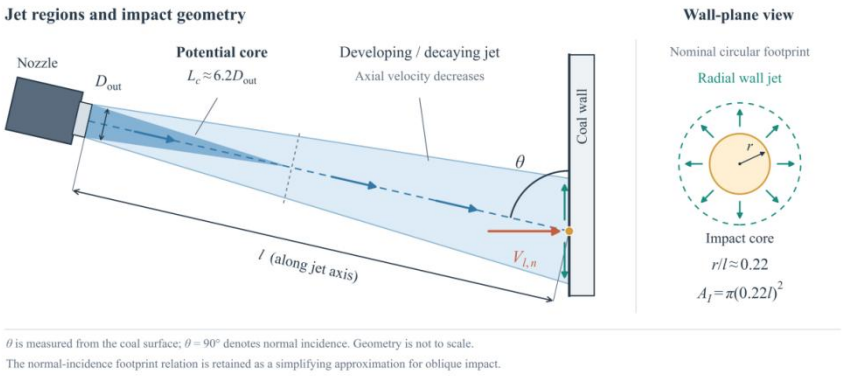


Fig. 2 Four key parameters and the combined impact-pressure model

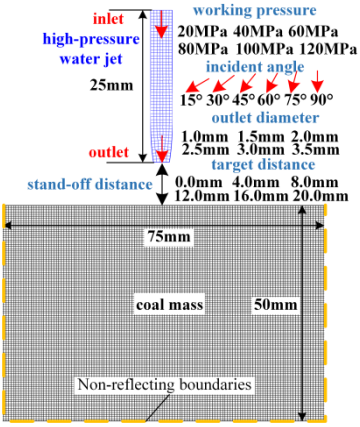


Fig. 3 Numerical model and core variable system of coal breaking by HPWJ impact

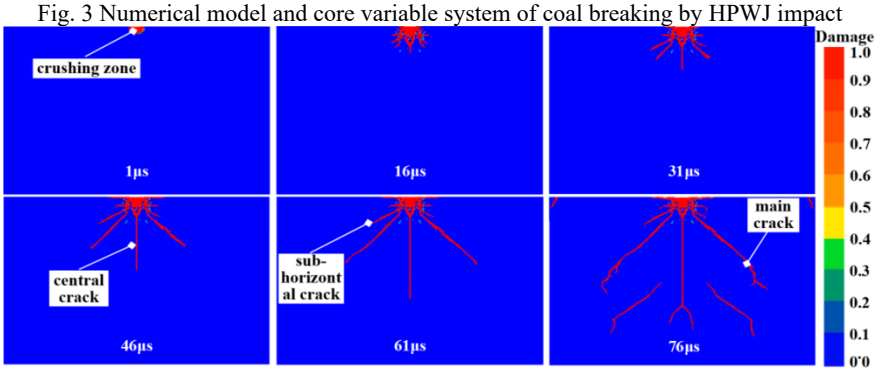


Fig. 4 Crack evolution process of coal breaking induced by HPWJ impact

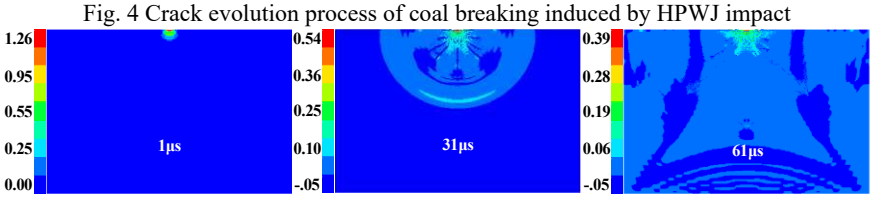
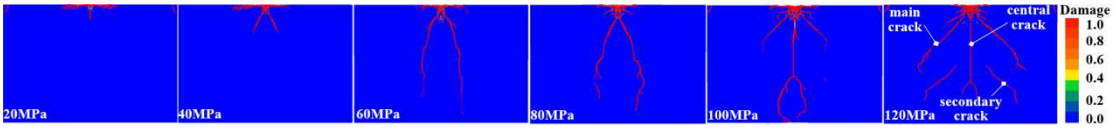
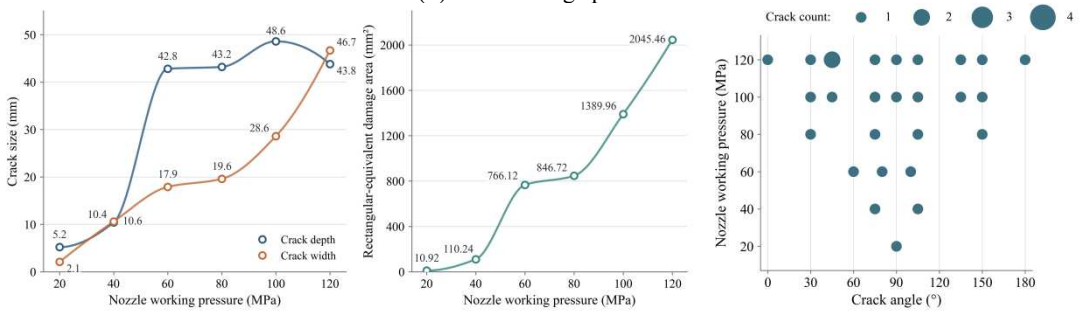


Fig. 5 Stress propagation and evolution during HPWJ coal breaking (color scale: × 10^4MPa)

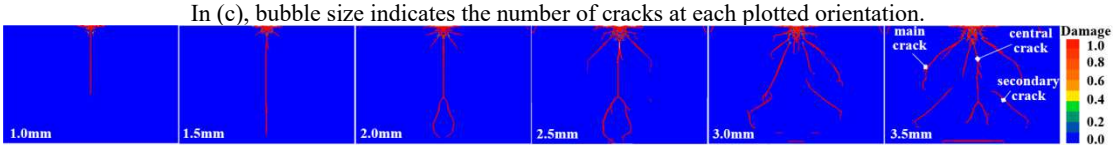


(a) Final damage patterns

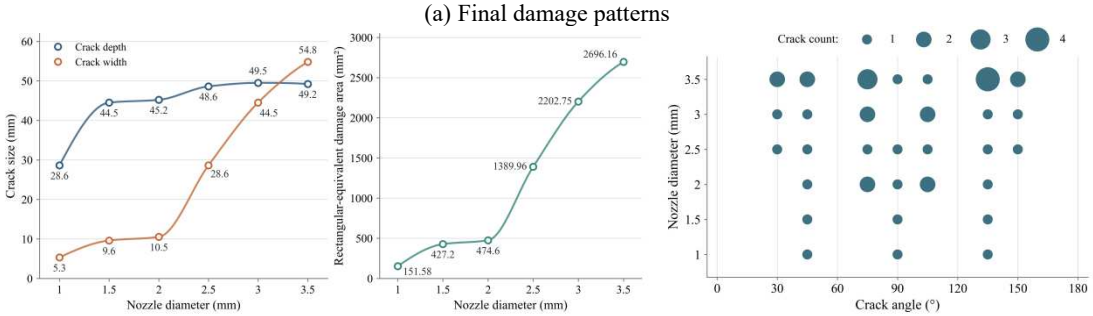


(b) Crack dimensions and rectangular-equivalent damage area (c) Crack angle and number

Fig. 6 Comparison of crack development in coal breaking under nozzle working pressures of 20–120 MPa. In (b), the curves are shape-preserving cubic interpolations through the plotted data points, used only as guides to the eye. In (c), bubble size indicates the number of cracks at each plotted orientation.

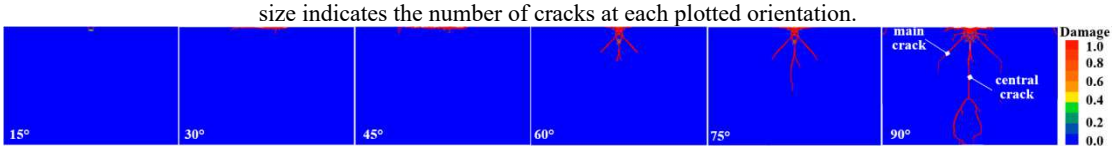


(a) Final damage patterns

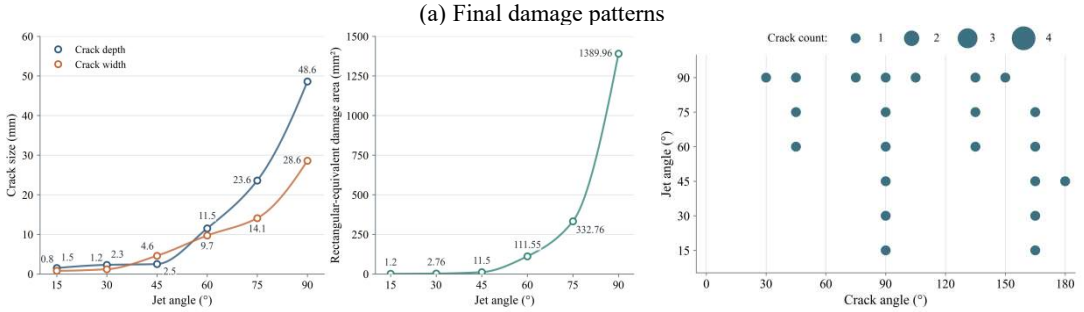


(b) Crack dimensions and rectangular-equivalent damage area (c) Crack angle and number

Fig. 7 Comparison of crack development in coal breaking under jet diameters of 1.0–3.5 mm. In (b), the curves are shape-preserving cubic interpolations through the plotted data points, used only as guides to the eye. In (c), bubble size indicates the number of cracks at each plotted orientation.

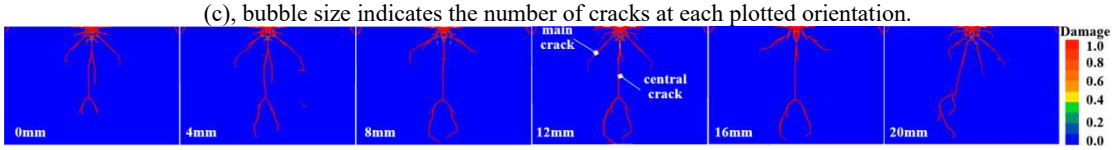


(a) Final damage patterns

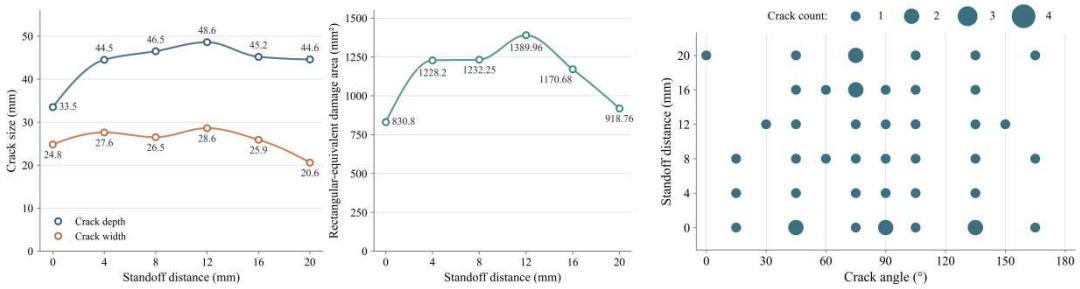


(b) Crack dimensions and rectangular-equivalent damage area (c) Crack angle and number

Fig. 8 Comparison of crack development in coal breaking under nozzle incident angles of 15°–90°. In (b), the curves are shape-preserving cubic interpolations through the plotted data points, used only as guides to the eye. In (c), bubble size indicates the number of cracks at each plotted orientation.



(a) Final damage patterns



(b) Crack dimensions and rectangular-equivalent damage area (c) Crack angle and number

Fig. 9 Comparison of crack development in coal breaking under stand-off distances of 0–20 mm. In (b), the curves are shape-preserving cubic interpolations through the plotted data points, used only as guides to the eye. In (c), bubble size indicates the number of cracks at each plotted orientation.

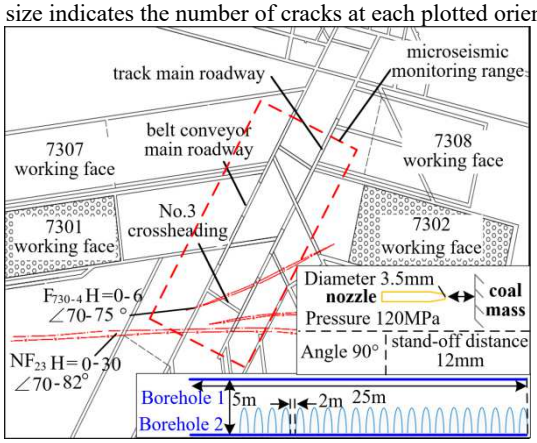


Fig. 10 Layout of high-pressure water jet slotting for pressure relief

Table 1 Constitutive parameters of coal materials

Parameter	Value	Parameter	Value
Initial density	1400 kg/m³	Maximum fracture strength ratio	0.25
Uniaxial compressive strength	21.1 MPa	Fracture strength exponent	0.61
Uniaxial tensile strength	4.45 MPa	Poisson's ratio	0.28
Bulk modulus of intact coal	2.411 GPa	Polynomial EOS constant K_1	2.41 GPa
Shear modulus of intact coal	1.24 GPa	Polynomial EOS constant K_2	-2.26 GPa
Hugoniot elastic limit (HEL)	4.5 GPa	Polynomial EOS constant K_3	772.41 GPa
Intact strength constant	0.70	hydrostatic tensile limit	-54 MPa
Intact strength exponent	0.61	Damage constant D_1	0.005
Strain rate coefficient	0.005	Damage constant D_2	0.7
Fracture strength constant	0.25	Bulking factor	0.5

Table 2 Statistics of microseismic events before and after pressure relief

Date	Status	Frequency	Total energy/J	Daily frequency	Microseismic energy level statistics		
					Energy level	Frequency	Percentage
13–19 June 2020	Before pressure relief	28	2.49E+04	4	High-energy level	7	25.0%
					Low-energy level	21	75.0%
21–27 June 2020	After pressure relief	19	1.52E+04	2.71	High-energy level	3	15.8%
					Low-energy level	16	84.2%

Supplementary Files

This is a list of supplementary files associated with this preprint. Click to download.

- SupplementaryData1.xlsx